International Journal of Microwave and Wireless Technologies

cambridge.org/mrf

Enhancing dual-band monopole antenna performance with a flexible compact design and a unique AMC cell

Elie Zaraket, Ludivine Fadel, Yéro Dia, Valérie Vignéras and Laurent Oyhénart

Laboratoire de l'Intégration du Matériau au Système (IMS), CNRS, UMR 5218, Université de Bordeaux, Bordeaux INP, Talence Cedex, Bordeaux, France

Research Paper

Cite this article: Zaraket E, Fadel L, Dia Y, Vignéras V, Oyhénart L (2025) Enhancing dual-band monopole antenna performance with a flexible compact design and a unique AMC cell. *International Journal of Microwave and Wireless Technologies*, 1–12. https://doi.org/10.1017/S1759078725000522

Received: 1 September 2024
Revised: 6 April 2025
Accepted: 19 April 2025

Keywords:
artificial magnetic conductor (AMC); dual-band system; electrically small antennas (ESA); flexible; GSM band; monopole antenna; WiFi band

Corresponding author: Elie Zaraket;
Email: elie_zaraket@hotmail.com

Abstract

This paper presents an effective approach to a compact antenna system incorporating a single artificial magnetic conductor (AMC), designed to operate in the GSM and WiFi frequency bands. The proposed system features a dual-band AMC single element measuring 60×60 mm^2 with $\pm 90^\circ$ bandwidths of 100 and 170 MHz. A comprehensive parametric study was conducted to optimize performance and determine the AMC phase while maintaining the compact size of the antenna system. Significant improvements in gain were observed, from −1.61 to 1.88 dBi at 0.9 GHz and from 3.33 to 5.66 dBi at 2.45 GHz. Additionally, the complete system achieves a compact electrical size of $0.18\lambda_0 \times 0.18\lambda_0 \times 0.048\lambda_0$, with an increased front-to-back ratio of 12.3 and 19.9 dB at both frequencies. Finally, measurements of the fabricated prototype show good agreement with the simulation results.

Introduction

Flexible, wearable, and compact electronics have rapidly evolved over the last decade, transforming diverse applications and technological interactions [1]. With the ability to bend, stretch, and conform to various shapes, wearable electronic devices are revolutionizing both medical and nonmedical industries [2].

On the other hand, compact electronics are crucial in health-care field where small size and precision are essential [3]. In Internet of things (IoT) applications, they can be easily embedded into various objects and environments, enabling seamless connectivity and data collection. Additionally, smaller devices can lower overall costs by using fewer materials and simplifying production processes [4]. For instance, the study in [5] presents a smartphone device equipped with six different antennas, catering to various standards (GPS, Bluetooth, WiFi, GSM, etc.).

To achieve a compact and high-performing antenna in wireless body area network (WBAN) and energy harvesting applications, the antenna dimensions are primarily governed by electrically small antenna (ESA), which was firstly introduced by Wheeler in 1947 [6]. Several ESA techniques are highly effective, including geometric alterations such as adding slots or slits, folded antennas, and short circuits [7]. Additionally, the use of magneto-dielectric materials and the integration of metamaterials, particularly in patch antennas, were explored [8]. Another approach involved adding localized loads or segments of conductive line (capacitive or inductive) to artificially increase the electrical length of the antenna, thus lowering its resonant frequency [9, 10]. However, these miniaturization techniques often result in significant performance drawbacks, especially in the sub-GHz bands [11]. The complexity and non-planarity of folded antenna geometries frequently result in reduced gain and directivity. Furthermore, their low efficiency increases the back-lobe levels, as demonstrated in various studies [7, 10]. This is primarily due to the absence of a standardized design procedure. In addition, the use of high dielectric material substrates for low-frequency designs significantly limits bandwidth and incurs high costs [12]. Metamaterial integration also results in very low gain and impedance bandwidth [13]. Consequently, most ESAs exhibit limited bandwidths and radiation efficiency, while those with wider bandwidths, higher gain, and improved efficiency tend to have lower miniaturization factors.

To address these challenges, integrating artificial reflectors based on metasurfaces offers a balanced solution by maintaining performance while reducing electrical size. These structures consist of periodic arrays of sub-wavelength scatterers, which significantly enhance antenna performance in terms of gain, impedance bandwidth, and front-to-back ratio (FBR) [14]. Moreover, artificial magnetic conductor (AMC) structures are particularly beneficial for improving antenna performance and reducing electromagnetic absorption by the human body [15].

In this work, we demonstrate a parasitic element (PE) behavior inspired by AMC properties, combining the advantages of both PEs and AMCs, an approach rarely explored

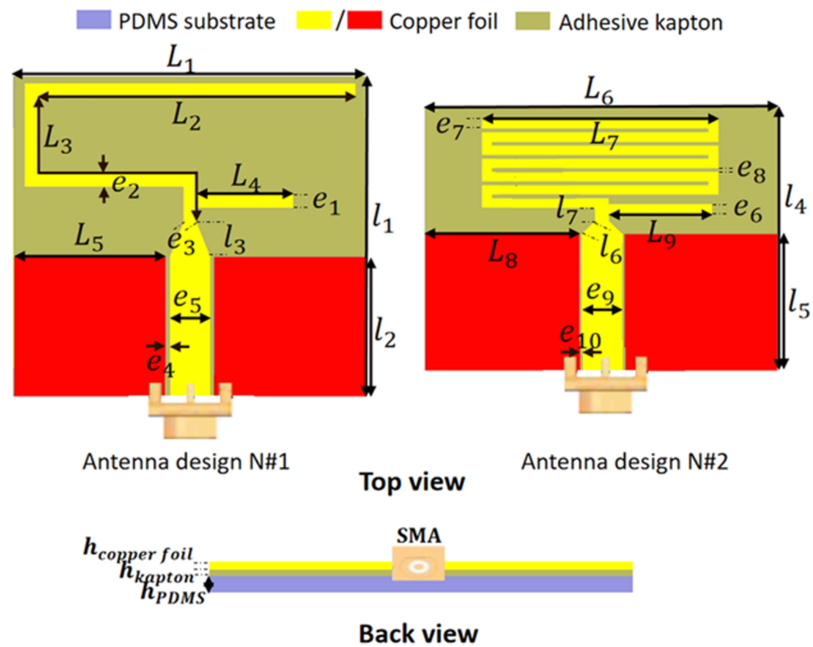

Figure 1. Comparison of the two CPW-fed monopole antenna configurations and their geometrical dimensions (in mm): $L_{1,6} = 50$, $L_2 = 48$, $L_3 = 48.5$, $L_4 = 15.5$, $L_{5,8} = 21.83$, $L_7 = 33.5$, $L_9 = 14.7$, $l_1 = 50$, $l_{2,5} = 20.75$, $l_3 = 3.7$, $l_4 = 40$, $l_6 = 3.7$, $l_7 = 2$, $e_1 = 2$, $e_{2,3,6,7} = 1.5$, $e_{4,10} = 0.25$, $e_{5,9} = 5.84$, $e_8 = 0.5$, $h_{\text{copper foil}} = 0.06$, $h_{\text{Kapton}} = 0.05$, $h_{\text{PDMS}} = 0.5$.

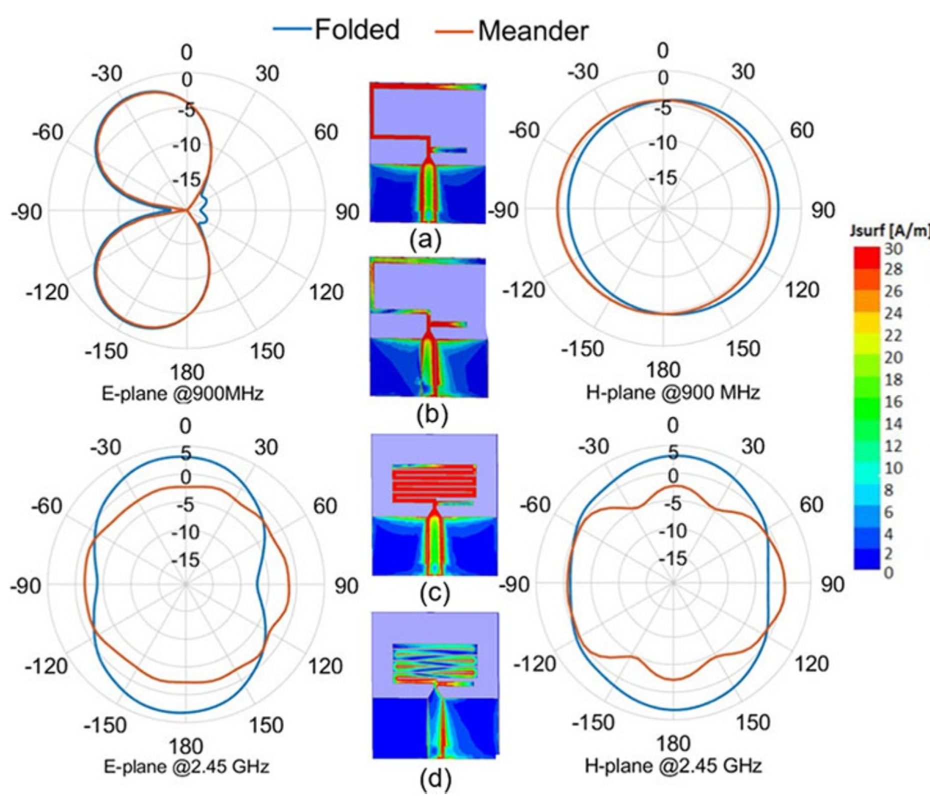

Figure 2. Radiation patterns and current distribution of the folded and meander antennas in both planes: (a) & (c) at 900 MHz; (b) & (d) at 2.45 GHz, respectively.

in current research. For instance, recent studies [16, 17] have demonstrated novel AMC unit cells utilizing rhomboid coupled parasitic patches and techniques involving planar parasitic patches and stacked elements.

This article proposes a compact, flexible dual-band antenna design with a PE-inspired AMC, covering the GSM band (880–990 MHz) and the WiFi band (2.25–3.22 GHz). The Section "Comparison of Two Proposed Antenna Configurations" compares the performances of two compact monopole antennas fed by a coplanar waveguide (CPW). The Section "Two Proposed AMC Variants" focuses on the configuration of the proposed AMC designs. In addition, this Section conducts a parametric study of the designed single element to identify the AMC and PEC (perfect electric conductor) phase regions. The fabrication process of the designed system is thoroughly detailed in the Section "Fabrication Steps for Antenna with AMC", while the Section "Measurement and Analysis" characterizes the complete system with the AMC and under bending conditions. The final section

https://doi.org/10.1017/S1759078725000522 Published online by Cambridge University Press

Table 1. Comparison of two compact dual-band antennas with different parameters

Parameter compact antenna	Folded antenna	Meander antenna
Resonant frequency (GHz)	0.914/2.49	0.896/2.47
Electrical size (*ka*)	0.66	0.6
Impedance bandwidth (MHz)	100/970	60/35
Peak return loss (dB)	−20.3/−36.5	−28.6/−18
Peak gain (dBi)	−1.25/3.33	−1.62/−0.58
Front-to-back ratio (FBR) (dB)	0.11/0.56	0.6/2.45
Radiation efficiency (%)	98/98	97/80

discusses the contribution of the novel prototype to the concept of ESA comparing it with the classical approach and existing works.

Comparison of two proposed antenna configurations

The design of a conformable and wearable dual-band antenna on polymer substrates necessitates meticulous selection of a miniaturization technique, ensuring optimal performance at both operating frequencies. Figure 1 shows two selected designs for the dual-band monopole antennas, labeled N#1 and N#2. These designs are inspired by the conventional CPW monopole antenna [18].

The two compact antennas, each consisting of two resonant paths, are designed to operate at low frequency using $L_{2,7}$ and at high frequency using $L_{4,9}$. The theoretical values of the aforementioned parameters are determined using the following equation:

$$L_{2,4} = \frac{c}{4f_{1,2}\sqrt{\epsilon_r}} \tag{1}$$

where $f_{1,2}$, c, and ϵ_r represent the low and high frequency, the speed of light, and relative permittivity of the polydimethylsiloxane (PDMS) substrate, respectively. The theoretical lengths of L_2 and L_4 are 49.90 and 18.33 mm. After optimization with a high frequency structure simulator (HFSS) Optimetrics, L_2 and L_7 were set to 48 mm and 33.5 mm at 900 MHz and L_4 and L_9 to 15.5 mm and 14.7 mm at 2.45 GHz, respectively.

The parameters $e_{1,6}$, $e_{2,7}$, $e_{5,9}$, and $l_{2,5}$ were optimized to increase the impedance bandwidth of each antenna while maintaining a compact electrical size. Antenna N#1 is a threefold monopole antenna with a length of $0.285\lambda_{900M}$ to which a stub of $0.13\lambda_{2.45G}$ is added. However, antenna N#2 is a meander antenna with a length of $0.66\lambda_{900M}$ and a spacing e_8 of 0.5 mm, connected to a stub of $0.12\lambda_{2.45G}$. The antenna structures are fed using a 50 Ω CPW line, with theoretical calculations based on paper [19]. The flexible substrate is made of PDMS, a transparent polymer with well-characterized dielectric properties of $\epsilon_r = 2.8$ and $\tan\delta = 0.008$. A 65 μm-thick polyimide, adhesive Kapton is then added above the PDMS layer to improve the cohesion robustness of the overall antenna.

The radiation patterns and surface current distribution were plotted in Fig. 2 for each compact antenna. The folded design presents a classical omnidirectional radiation pattern in the H-plane at 900 MHz and 2.45 GHz. The E-plane radiation pattern at the lower frequency is asymmetrical due to the influence of the designed folded arm, which is oriented to one side of the surface, and the optimized length of the CPW line. At higher frequency, the antenna's radiation is more symmetry radiated in the both planes.

The reduced electrical size of the antenna design N#1 ($ka = 0.66$, where a is the radius of the minimum enclosing sphere and k is the wave number) limits its radiation performance before integrating the single AMC element, particularly at sub-GHz frequencies. The results thus show a maximum gain (E-plane) of −1.25 and 3.33 dBi, a reflection coefficient S_{11} of −20.3 and −36.5 dB, and an impedance bandwidth of 100 and 970 MHz for the two operating resonant frequencies, respectively. Nevertheless, the meander antenna N#2 exhibits an insufficient maximum gain of −1.61 and −0.58 dBi, with a matched S_{11} and narrower impedance bandwidths of 60 and 35 MHz at 0.896 and 2.47 GHz. This is due to the proximity of the meander line to the

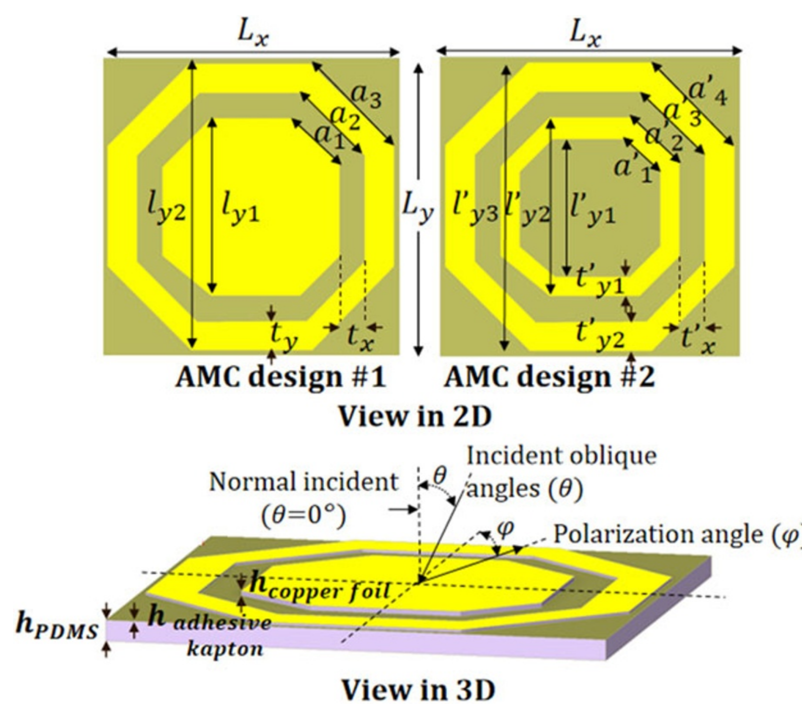

Figure 3. Configuration of the two AMC cells: octagonal ring centered with a patch octagon (AMC design #1) and two octagonal rings (AMC design #2). Geometrical dimensions (in mm): $L_x = L_y = 60$, $l_{y1} = 37.48$, $l_{y2} = l'_{y3} = 58.94$, $l'_{y1} = 20.18$, $l'_{y2} = 30.67$, $t_x = 4.62$, $t_y = 7.3$, $t'_x = 7.85$, $t'_{y1} = 5.15$, $t'_{y2} = 6.28$, $a_1 = 15.3$, $a_2 = 18.37$, $a_3 = a'_4 = 24.41$, $a'_1 = 8.36$, $a'_2 = 12.7$, $a'_3 = 19.21$.

https://doi.org/10.1017/S1759078725000522 Published online by Cambridge University Press

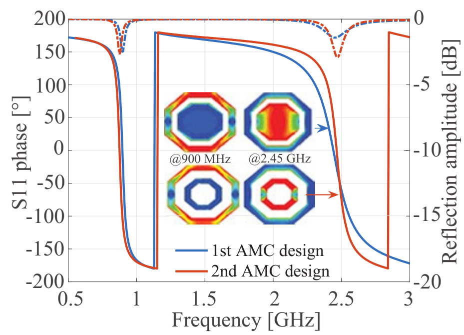

Figure 4. S_{11} phase and magnitude followed by the surface current distributions of the two dual-band AMC cells.

Table 2. Comparison of two AMC variants with different parameters

Parameter AMC design	Design #1	Design #2
Frequency of S_{11} zero phase (GHz)	0.896/2.44	0.875/2.46
Dimension (λ_0^3)	0.18 × 0.18 × 0.016	0.18 × 0.18 × 0.016
Bandwidth within $\pm 90^\circ$ (%)	4.24/8.57	4/4.3
Reflection amplitude (dB)	−2.49/−1.4	−2.67/−2.9

λ_0: free-space wavelength computed at low-frequency band.

2.45 GHz stub, which induces undesired electromagnetic coupling, represented by parasitic capacitors. This results in reduced antenna efficiency (80%) and gain, a narrower bandwidth, and a disruption of radiation pattern symmetry within the 2.45 GHz frequency range. This is confirmed by the weak current concentration on the 2.45 GHz resonant stub, as illustrated in Fig. 2d. The FBRs, measured from the main lobe ($\theta = 0^\circ$) to the back-lobe ($\theta = 180^\circ$), are below 2 dB for both antenna designs. As shown in Table 1, this limitation poses a significant challenge for future advancements in on-body applications.

Two proposed AMC variants

Once the folded CPW monopole antenna is selected, two AMC patterns are proposed: AMC design #1 consists of a parasitic octagonal ring that affects the lower resonant frequency, centered by a patch octagon to resonate at the higher frequency. On the other hand, a second variant, AMC design #2, forms two octagonal rings, as shown in Fig. 3.

The adjustment of the truncated corners aims to reduce the period of the cell surface to 60 × 60 mm^2 with $L_x = L_y$ less than $\lambda_{900\text{M}}/4$. Adjusting the t_x gap between the two octagonal patterns induces slight rightward shifts in the frequency of S_{11} phase. This shift is linked to variations in the t_y parameter, resulting in instability of zero phase of S_{11} around 900 MHz. Remarkably, no such instability is discerned at 2.45 GHz. The reverse case involves adjustments to the l_{y1} parameter. The thickness of the AMC substrate (5.5 mm $<< \lambda$) impacts the $\pm 90^\circ$ bandwidth of the S_{11} phase, particularly at lower frequency. For pattern #2, the optimization primarily targeted the parameter l'_{y1}, which has the most pronounced impact on the performance of S_{11} phase at 2.45 GHz, along with the gap t'_x, and the width t'_{y2} for optimal performance at 900 MHz.

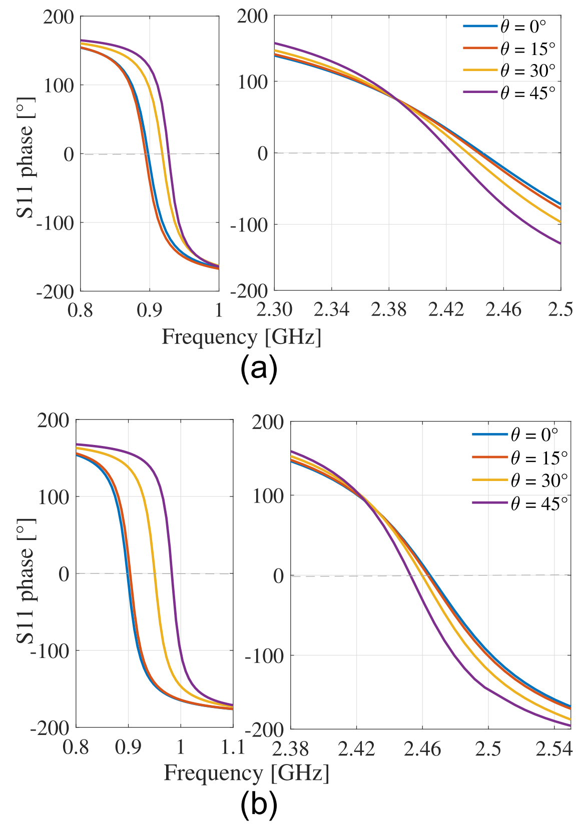

Figure 5. Effect of the variation of oblique incidence angles (θ) on the S_{11} phase behavior of (a) design #1 and (b) design #2 in TE/TM polarization at both frequencies. (a) AMC design #1 and (b) AMC design #2.

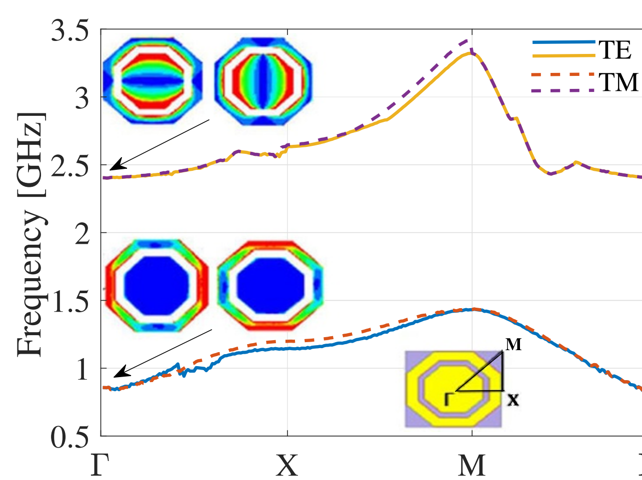

Figure 6. Dispersion diagrams for TE and TM modes at 900 MHz and 2.45 GHz, centered on Γ.

Each AMC cell was simulated independently in Ansys HFSS using periodic boundary conditions. As a result, the S_{11} phases of the two AMCs overlap at around 900 MHz, as depicted in Fig. 4. Both patterns fall within the AMC phase range of $\pm 90^\circ$, as illustrated in Table 2, at both low and high frequencies. At 2.45 GHz, AMC #1 exhibits a broader bandwidth (8.57%) compared to AMC #2 (4.3%). This bandwidth sensitivity is influenced by variations in

https://doi.org/10.1017/S1759078725000522 Published online by Cambridge University Press

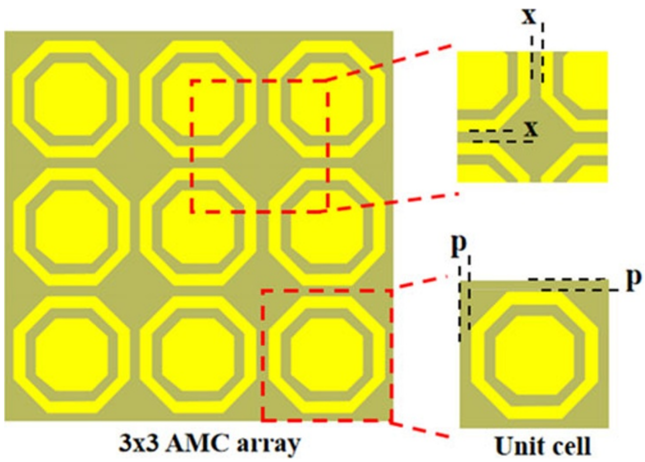

Figure 7. Study of the impacts of parameters *p* and *x* on AMC phase characteristics.

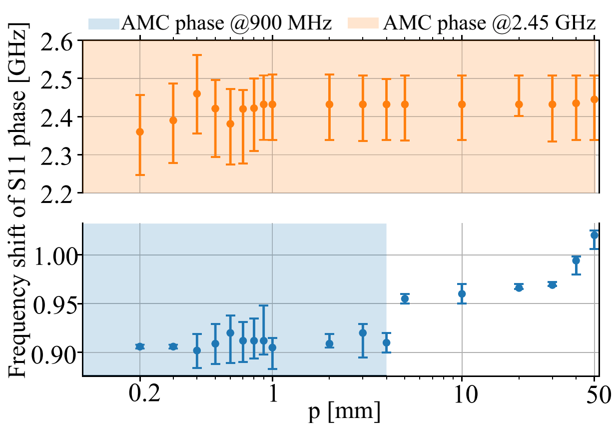

Figure 8. Impact of parameter *p* on frequency shift and bandwidth of the S_{11} phase in a single AMC cell.

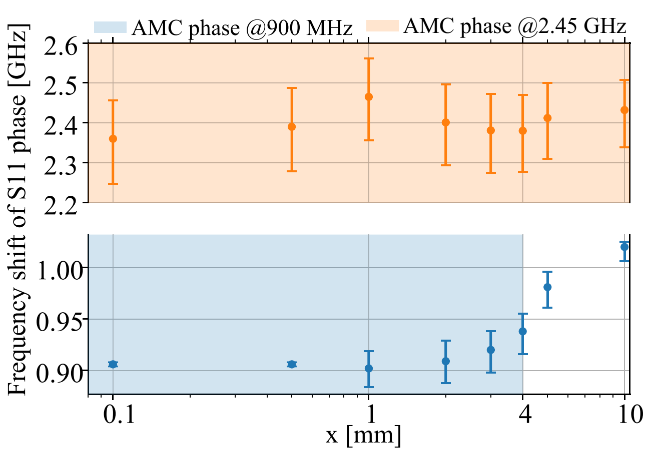

Figure 9. Impact of parameter *x* on frequency shift and bandwidth of the S_{11} phase in the AMC array.

the thickness of the AMC substrate (h_{PDMS}) and parameters such as the widths of the octagonal patch and ring: l_{y1}, t_y, t'_{y1}, and t'_{y2}.

Figure 5 illustrates a comparison of the effect of oblique incident angles on the S_{11} phase of AMC designs #1 and #2 in TE/TM polarizations. At 2.45 GHz, as the angle of incidence increases from 0° to 45°, both patterns exhibit a similar frequency shift, with slight variations of 0.45% for AMC #1 and 0.53% for AMC #2. The stability of the zero phase at 2.45 GHz is evident in the dispersion diagram for AMC #1 pattern, as depicted in Fig. 6. It is observed in the dispersion diagram, Fig. 6, where the curves remains nearly flat along Γ-X around 2.45 GHz. The bandwidth decreases by approximately 2.95% (Fig. 5a) and 1.43% (Fig. 5b) with increasing oblique incidence angles.

However, at 900 MHz, AMC #2 falls out of the AMC phase at $\theta = 30^\circ$ and 45°, causing a frequency shift of the S_{11} zero phase by 60 and 86 MHz, respectively. This phenomenon is attributed to the movement observed in the dispersion diagram, where the branch corresponding to 900 MHz shifts toward higher frequencies, greater than 1 GHz, with an increase in the angle, along Γ-X. This shift also impacts the AMC bandwidth, resulting in a decrease of 1.21% and 0.86% for AMC #2, respectively. These previous results suggest that the octagonal ring centered with a patch octagon offers stable performance and is, therefore, preferred for combining with the folded monopole antenna.

The operating frequencies of the AMC #1 structure have been further investigated through the analysis of the dispersion diagram, as shown in Fig. 6. The electric field magnitude was plotted for two specific branches, encompassing TE and TM modes at 900 MHz and 2.45 GHz at Γ. At the first branch, there is a nearly degenerate behavior on Γ-X-M-Γ. Conversely, in the case of the 2.45 GHz branch, the lifting of degeneracy began after the second third of Γ-X, and the frequency dispersion remains low over the first third of X-M. Consequently, it can be deduced that for angles less than 60°, Fig. 5a, the phase shift for these modes is expected to undergo only marginal changes. The absence of band gaps is attributed to the absence of the vias.

Parametric study of the PE inspired by AMC

This parameter study reveals the behavior of the designed single AMC element under ideal periodic conditions. It identifies which cell geometry, operating at 900 MHz and 2.45 GHz, is more sensitive to AMC phase perturbations.

The parameter *p* represents the distance between the edge of the cell and the AMC pattern, as shown in Fig. 7. This parameter exhibits a smooth impact at 2.45 GHz on the $\pm 90^\circ$ bandwidth within which the frequency of the S_{11} zero phase remains in the AMC phase throughout the variation of *p*, as shown in Fig. 8. However, a parasitic behavior is detected at the outer octagonal ring operating at 900 MHz, where the S_{11} zero-phase frequency shifts by 60 MHz, exceeding the AMC phase bandwidth and thus entering the PEC phase when *p* surpasses the range of 0.1–4 mm.

Further parametric analysis of the AMC structure, illustrated in Fig. 7 as a 3×3 AMC array, investigates the effects of the parameter *x*, which denotes the equidistant gaps between adjacent cells. As shown in Fig. 9, the variation of parameter *x* from 0.1 to 10 mm introduces a notable degree of sensitivity, particularly at a frequency of 900 MHz. The frequency shift of the S_{11} phase exceeds the AMC phase $\pm 90^\circ$ to PEC phase by 4.4% when *x* surpasses 4 mm. However, at 2.45 GHz, the AMC phase exhibits a slight fluctuation in frequency shift, with a variance of $\pm 3\%$. Conversely, at 900 MHz, the AMC phase bandwidth is minimal at $x = 0.1$ and 0.5 mm ($\pm 0.5\%$) but increases to 4% when *x* exceeds 1 mm.

Therefore, this analysis reveals that the outer octagonal ring geometry of the AMC cell operating at 900 MHz shows greater sensitivity in the AMC phase compared to the performance at 2.45 GHz. Thus, to ensure the AMC phase of the designed cell, the parameters *p* and *x* should remain within the range of 0.1–4 mm.

https://doi.org/10.1017/S1759078725000522 Published online by Cambridge University Press

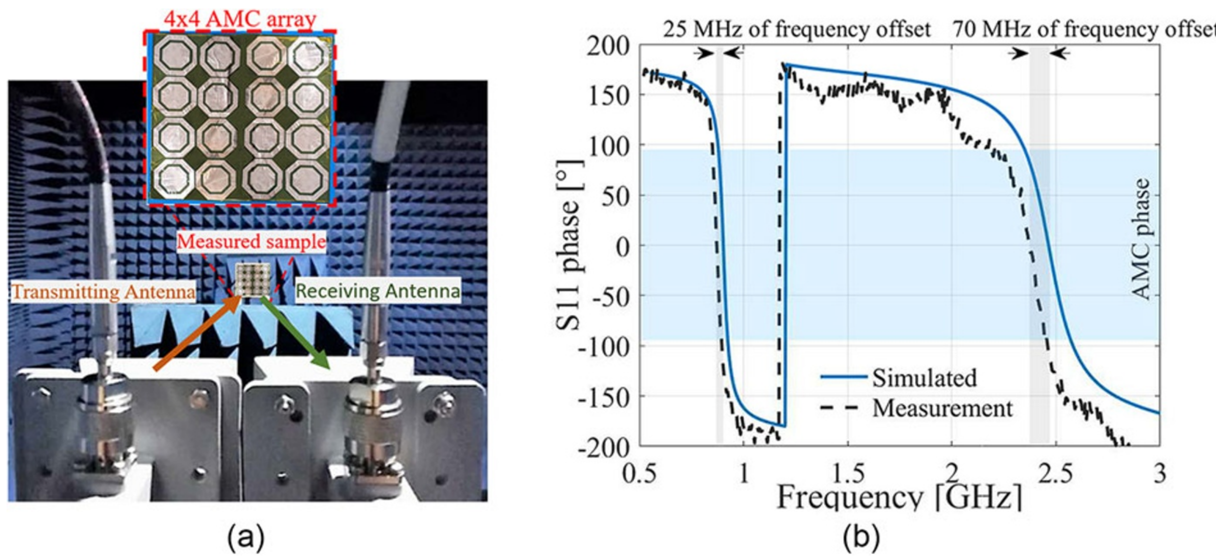

Figure 10. Measurement setup of the S_{11} phase of 4 × 4 AMC array: (a) in anechoic chamber; (b) comparison of S_{11} phase between measured and simulated results.

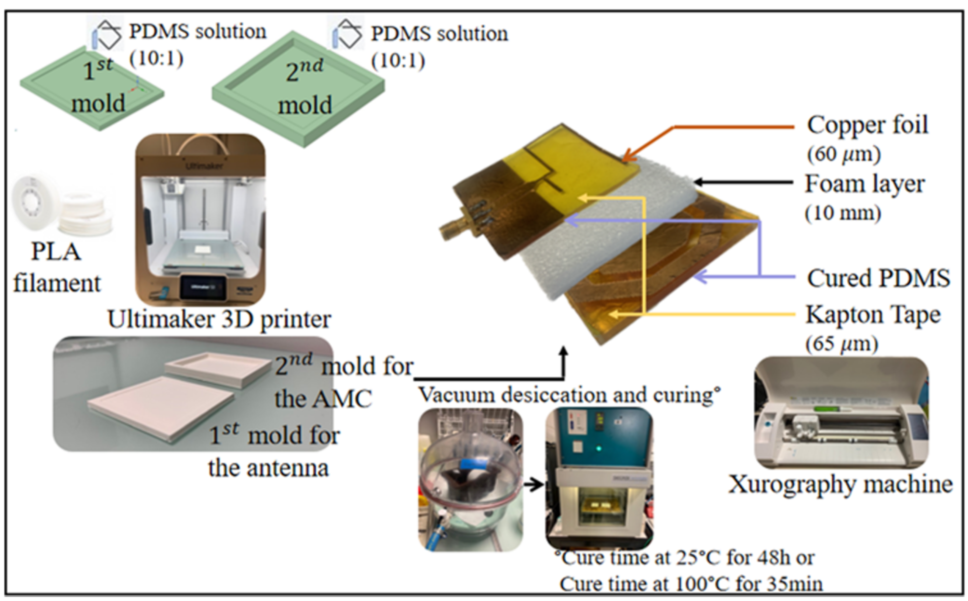

Figure 11. Fabrication process of the antenna system.

Experimental results

A 4 × 4 AMC prototype was fabricated using a Xurography machine [20]. The measurement process of the S_{11} phase for the AMC array was conducted in an anechoic chamber [21], as illustrated in Fig. 10a, starting with a PEC metallic plate of identical dimensions (240 mm × 240 mm) as the reference.

According to Fig. 10b, the measured resonance frequencies are 0.871 GHz and 2.37 GHz, while the simulation predicts frequencies of 0.896 GHz and 2.44 GHz, resulting in deviations of −2.8% for both resonant frequencies. The measured AMC's operational bandwidths, with differences of 15% and 5%, exhibit a high degree of concordance with the simulation results. The discrepancy between the measured and expected results can be attributed to two main factors. First, the two horns were not positioned strictly at normal incidence but at an incidence angle of approximately 10°. Secondly, mechanical challenges occur when a given small support is not entirely attached to the fabricated 4 × 4 AMC array substrate composed of adhesive Kapton and PDMS.

Fabrication steps for antenna with AMC

As mentioned in Section II, PDMS is the chosen material with measured $\epsilon_r = 2.80$ and $\tan\delta = 0.008$ that allows us to overcome the challenges of communicating with wearable and conformable object. In addition, due to its mechanical adaptability, ease of manufacturing, and stable chemical properties [22], the PDMS layer of the PE inspired by AMC also serves as an alternative substrate to foam, reducing the distance between the AMC scatterer and the ground plane. In contrast, the PDMS is recognized for being hydrophobic and chemically inert material. Hence, this polymer substrate demonstrates limited adhesion to metallic surfaces and conductive inks. The single element backed-antenna is

https://doi.org/10.1017/S1759078725000522 Published online by Cambridge University Press

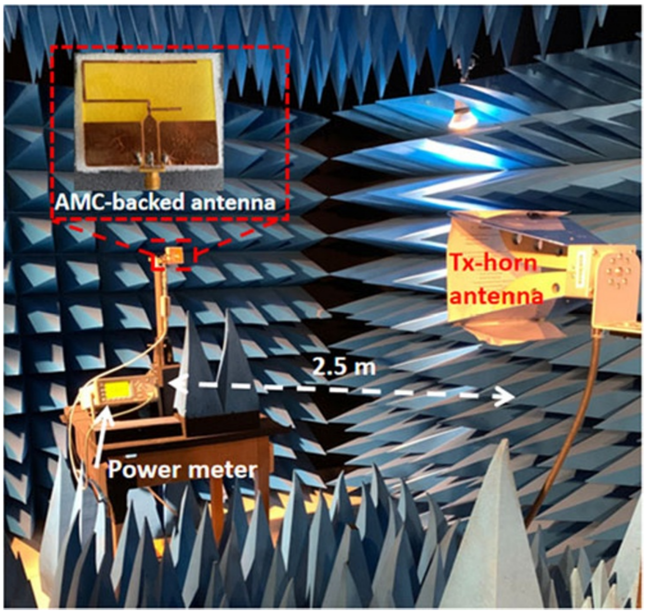

Figure 12. Measurement setup of the folded monopole antenna with a single element backing in anechoic chamber.

thus assembled by bonding the antenna, fabricated on an adhesive Kapton film (65 μm), with $\epsilon_r = 3.2$ and tan$\delta = 0.0017$ [23], to the top surface of the PDMS, Fig. 11.

The PDMS substrate (Sylgard 184) is a mixture consisting of the monomer and the curing agent in a ratio of 10:1. Before curing, a degassing step is necessary to remove all bubbles from the solution. The desired thicknesses are 5.5 mm and 0.5 mm for the AMC and the antenna patterns, respectively. To achieve these thicknesses, molds were created using a 3D printer, specifically the Ultimaker, with a polylactic acid (PLA) substrate having $\epsilon_r = 2.22$ and tan$\delta =$ 0.005. All dielectric substrates employed in this study were characterized using the resonant cavity technique at both resonant frequencies [24].

The conductive parts are produced by etching a 60 μm-thick adhesive copper foil with an electrical conductivity of 5.96×10^7 S/m using the Xurography technique [20]. On top of the PDMS layer, a 65 μm-thick adhesive Kapton® is applied as an intermediate surface to which the copper foil is bonded. Figure 11 briefly illustrates all the steps in sequence and highlights the stacking of all the layers. The CPW is connected to the antenna feed point via a subminiature version A (SMA) connector.

Measurement and analysis

The folded antenna is coaxially fed and tested in the anechoic chamber, as shown in Fig. 12. The antenna system is placed at a far-field distance of 2.5 m to the Tx-horn antenna connected to an Agilent E4428C power generator.

The effect of the S_{11} performance is studied in Fig. 13 by positioning the single element in closer proximity to the antenna (ΔH). The measured S_{11} exhibits an unstable response at 2.45 GHz. The frequency shift of S_{11} remains 106 MHz for ΔH of 5 cm. Subsequently, it gradually decreases to 102 and 25 MHz as ΔH decreases to 3 and 1 cm, respectively, which ΔH is less than $\lambda_{2.45G}/4$, as shown in Fig. 13. Moreover, the bandwidth decreases from 858 MHz without AMC to 220 MHz at ΔH of 1 cm, which is

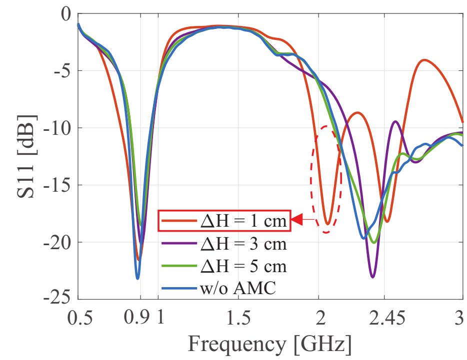

Figure 13. Measured S_{11} of the antenna system design with varying spacing ΔH beneath the antenna.

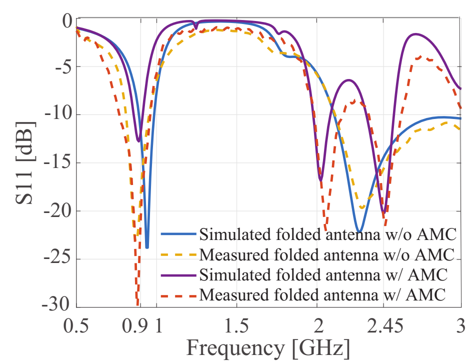

Figure 14. Simulated and measured S_{11} of the CPW-fed monopole antenna without/with AMC cell backing.

considered sufficient to cover the higher frequency. Nonetheless, the appearance of a third resonant frequency at 2.15 GHz can potentially be attributed to the proximity of the AMC cell at a distance of 1 cm, a scenario that does not occur for ΔH values greater than 1 cm. This is attributed to the close interference between electromagnetic waves from the radiator and the PE inspired by AMC, resulting in undesired resonant frequencies. Due to the fact that ΔH is less than $\lambda_{900M}/4$, the frequency shift of the S_{11} is stabilized. It shifts slightly around 37.5 MHz at 900 MHz, with a bandwidth of around 130 MHz for all the tested ΔH. With a ΔH of 1 cm, the overall antenna system exhibits a good impedance match ($S_{11} < -10$ dB), while maintaining a distance of less than $\lambda/4$ at both frequencies.

Figure 14 shows a good agreement of the simulated and measured S_{11} of the overall antenna system design. The folded antenna exhibits a 20 MHz left shift with an impedance bandwidth of 100 MHz at 900 MHz for both without and with AMC-backing. At higher frequency, the 10 dB bandwidth diminished from 970 to 170 MHz, this still encompasses the 2.45 GHz. However, the frequency shift of S_{11} is considered negligible. The slight discrepancy between the simulation results and measurements can be explained by the imperfections in the various stages of realization and soldering.

As illustrated in Fig. 15, the simulated and measured FBR are in agreement at both planes and frequencies. The measured FBR increased from less than 2 dB to 12.3 and 19.9 dB, with measured realized gains of 1.88 and 5.66 dBi and simulated radiation efficiencies of 95% and 88% at both frequencies, respectively. The undesired third frequency at 2.15 GHz

https://doi.org/10.1017/S1759078725000522 Published online by Cambridge University Press

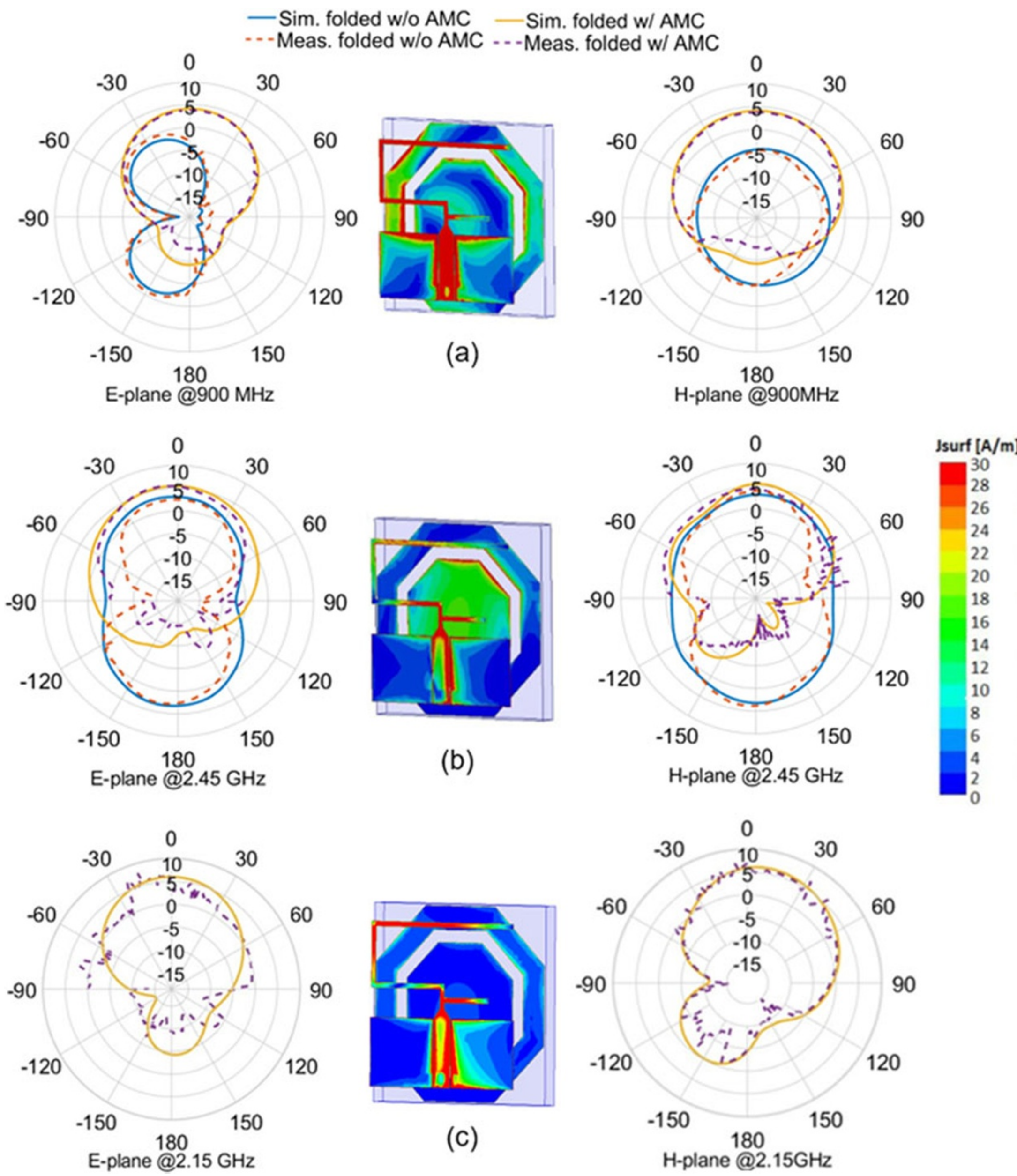

Figure 15. Comparison of the simulated and measured radiation patterns and current distribution of the antenna without/with AMC in both planes at 0.9 and 2.45 GHz and at the corresponding third resonant frequency of 2.15 GHz.

exhibits an impedance bandwidth of 132 MHz, a maximal gain of 6.01 dBi, and FBR of 14 dB. As seen in Fig. 15, the distribution of surface current on the antenna system is also depicted at frequencies of 900 MHz, 2.15 GHz, and 2.45 GHz.

The impact of bending test on the S_{11} performance of the complete system design was measured, as shown in Fig. 16. The antenna system was tested on the fabricated PLA objects with different radii, considering their dielectric properties during the simulation and measurement. A frequency shift of 60 MHz (6.66%) and 120 MHz (4.89%) in the x-direction and 50 MHz (5.55%) and 100 MHz (4.08%) in the y-direction was observed at 900 MHz and 2.45 GHz, respectively, when the antenna system was bent till a radius of 30 mm. However, for bending radii greater than 60 mm, most S_{11} frequency shifts were less than 20 MHz, ensuring that S_{11} remained well-matched.

As a result, the impact of a 60 mm bending radius shows stability in gain measurements and consistency with simulations, with peak measured gains of 1.45 and 5.44 dBi at 900 MHz and 2.41 GHz, respectively. However, a difference of ±1 dBi between the free space and bending tests is observed in Fig. 17a, particularly at the lower frequency. This discrepancy is attributed to unwanted mutual coupling between the antenna and the AMC single element caused by bending, which distorts the radiation pattern and reduces gain. This effect is also reflected in the FBR values, Fig. 17b, which are reduced by ±2–4 dB compared to those in free space at both frequencies. With FBR values exceeding 10 dB at both resonant frequencies, we can proceed to test

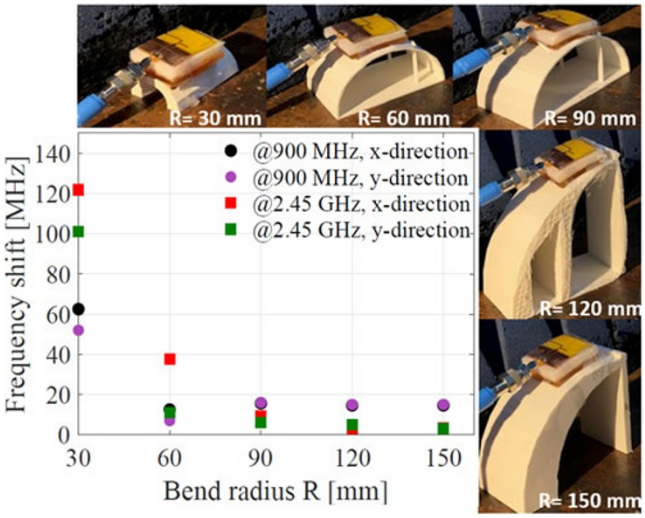

Figure 16. Measurement of S_{11} frequency shift under bending effects in both directions.

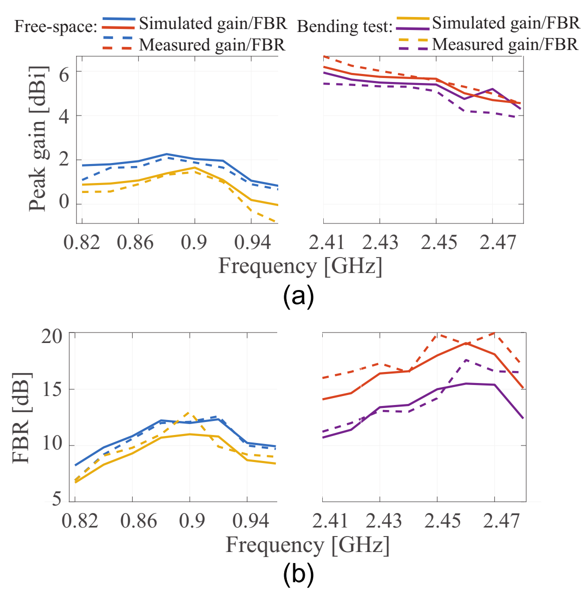

Figure 17. Simulated and measured peak realized gain (a) and FBR (b) in free space and during the bending test ($R = 60$ mm).

our final prototype on the human body for potential health-care applications.

Discussion and results

As demonstrated previously, a single AMC-backed antenna on two polymer substrates has demonstrated effective performance and significant size reduction, making it ideal for wearable health-care devices. Therefore, our prototype serves as a viable alternative to the classical approach (antenna + ground plane), as depicted in Fig. 18. The objective is to highlight the advantages of this alternative method compared to the classical approach in terms of electrical size and performance metrics.

In the classical approach, the antenna achieves constructive interference at a minimum space of $\lambda_0/4 = 83.3$ mm, with a_{GND} ranging from 60 to 500 mm, where λ_0 is the free-space wavelength at 900 MHz. The frequency shift of S_{11} remains relatively constant, within an impedance bandwidth (dashed curves) of ±100 MHz at 0.9 GHz and ±900 MHz at 2.45 GHz, as illustrated in Fig. 19a. Furthermore, in Fig. 19b and 19c, the maximum gain and FBR increase significantly as a_{GND} reaches approximately 250 mm at 2.45 GHz and 300 mm at 900 MHz.

On the other hand, a 10 mm spacing ($\lambda_0/33$) between the antenna and the AMC cell (60×60 mm^2), both simulated and measured, does not negatively impact the frequency shift of S_{11} compared to the classical approach. However, this spacing reduces the bandwidth from 11.7% to 6.1% at 900 MHz and from 39.2% to 11.4% at 2.45 GHz. As shown in Fig. 19b, the maximum realized gain at 900 MHz is significantly lower than that of the classical approach, primarily due to the use of a single AMC element and the sensitivity of the octagonal ring design on the antenna. However, there is a significant impact on the gain at 2.45 GHz compared to the classical approach, when ground size is increased to 175 mm. Lastly, the close proximity of the antenna and AMC cell results in a significantly higher FBR, as observed at 60 mm of a_{GND}.

Increasing the surface area of the artificial reflector, as illustrated in Fig. 18b, with $[n \times n]$ arrays, maintains a well-matched S_{11} and enhances the impedance bandwidths by more than 50% at 900 MHz and 11% at 2.45 GHz compared to a single AMC cell (Fig. 19a). The increased number of AMC cells results in notably higher FBRs at both frequencies. However, the maximum gain does not improve as much, particularly at 900 MHz, remaining below the classical approach. This is due to the proximity sensitivity of 10 mm, which causes electromagnetic noise and performance disturbances. Therefore, a single AMC cell can effectively cover the entire antenna, achieving a reduced electrical size of $ka = 0.79 < 1$ while maintaining satisfactory performance.

To complete the comparison of our final work with the existing studies summarized in Table 3, we have introduced figures of merit, $\mathrm{FOM}_{\{Gain,FBR,Q\}}$, which quantify the trade-offs between the gain, FBR, and the quality factor (Q) performances of the antenna system relative to its electrical size. These FOMs are defined in the following equation:

$$\mathrm{FOM}_{\{Gain,FBR,Q\}} = \frac{\{Gain, FBR, f_r/BW\}}{(k \cdot a)^2 \cdot (k \cdot h)} \tag{2}$$

with f_r being the resonant frequency at 900 MHz and 2.45 GHz, $k = 2\pi/\lambda_0$ the wavenumber, a the radius of the minimum sphere enclosing the antenna system, and h the air gap between the antenna and the AMC. In addition, $(k \cdot a)^2$ provides a measure of the effective aperture of the antenna system. The three FOMs are crucial for comprehensive antenna design and performance optimization, in terms of bandwidth efficiency, high directional gain, and effective suppression of back-lobes.

According to the table, our compact antenna system exhibits the smallest electrical size of 0.79, compared to the previous works. The FOM_Q shows a satisfactory value, particularly in the sub-GHz range, although it is lower than those reported in [29]. Nevertheless, using AMC properties have shown an improvement in FOM_{Gain} and FOM_{FBR}, achieving values of 15.85/47.71 and 103.75/167.89 at both frequencies, respectively, compared to other types of metasurface employed in the previous works such as [25, 27–29].

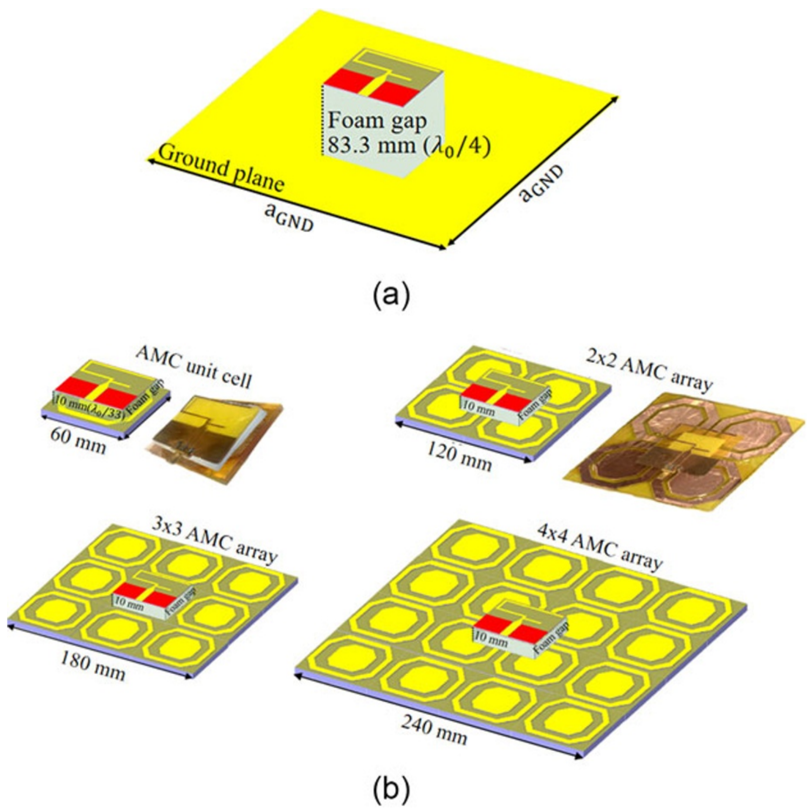

Figure 18. Simulation setup of the antenna system for the classical and alternative approaches with two manufactured prototypes. (a) Classical approach constructive interference and (b) alternative approaches.

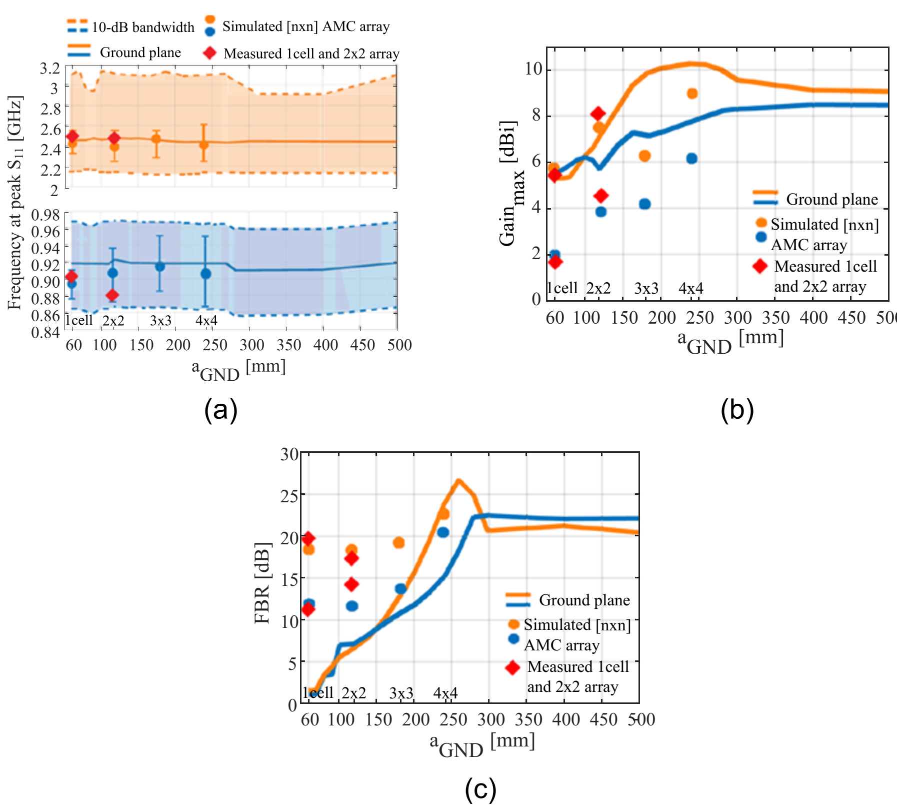

Figure 19. Comparison of the two approaches performance at different a_{GND} at 900 MHz (blue) and 2.45 GHz (orange): (a) frequency shift of peak S_{11}; (b) maximum realized gain; (c) FBR. The diamond red shapes represent the measured results for a single element and a 2 × 2 AMC array at both frequencies.

https://doi.org/10.1017/S1759078725000522 Published online by Cambridge University Press

Table 3. Comparison of reference antenna systems for wearable applications

Works, year	[25], 2014	[26], 2020	[27], 2020	[28], 2022	[29], 2023	[30], 2024	This work
Antenna topology	Monopole	Patch	Patch	Monopole	Patch	Loop antenna	CPW Monopole
f_r (GHz)	1.8 2.45	1.575 2.45	1 2.4	0.915 2.45	0.865 2.4	0.90	0.90 2.45
Electrical size (ka)	4	1.98	0.89	1.51	1.92	0.87	0.79
Flexibility	Yes	Yes	Yes	No	Yes	Yes	Yes
On AMC	No EBG	Yes 3 × 3	No EBG	Yes MTM*	No FSS	Yes 4 × 2	Yes AMC*
10 dB BW (%)	10.92 5.08	27 7.5	40 6.25	1.96 5.46	1.27 10.41	N/A	11.11 6.81
FOM_Q	3.78 8.15	18.02 19.58	75.21 482.10	41.53 14.90	117.90 14.35	N/A	75.94 123.86
Realized gain (dBi)	1.90 −0.50	1.98 1.94	2.23 2.38	2.87 6.8	5.31 8.30	−8	1.88 5.66
FOM_{Gain}	0.79 −0.19	2.70 2.64	67.10 71.63	2.34 5.53	7.95 12.42	−233	15.85 47.71
FBR (dB)	15.55 15.64	19.60 17.40	0.28 23.23	10.37 16.8	6 25.5	13	12.30 19.90
FOM_{FBR}	6.43 6.43	26.92 23.90	8.36 700.10	8.42 13.66	8.94 38.14	378.76	103.75 167.89

MTM*: metamaterial inspired AMC, AMC*: PE-inspired AMC.

Conclusion

A novel compact CPW-fed monopole antenna for IoT applications, featuring a single AMC cell, has been investigated through simulation, fabrication, and characterization in the GSM and WiFi bands. A parametric study showed that for parameters p and x beyond 4 mm, the AMC cell transitions to the PEC phase only at 900 MHz. Thereafter, the antenna system, with (ka = 0.79), was compared to a classical approach and to existing works in terms of electrical size and performance. The comparison has demonstrated superior $FOM_{\{Gain,FBR,Q\}}$, corresponding to the reduced electrical size at 0.9 and 2.45 GHz, respectively. The next phase involves testing our prototype under real-world conditions, including off-body constraints, for wearable health-care applications.

Acknowledgements. The author gratefully appreciates Jean-Luc Lachaud from the IMS Laboratory and David Bedenes from Bordeaux INP for their valuable contributions to fabrication techniques and measurement methods.

Competing interests. The authors report no conflicts of interest.

References

1. **Kazanskiy NL, Khonina SN, and Butt MA** (2024) A review on flexible wearables – Recent developments in non-invasive continuous health monitoring. *Sensors and Actuators A: Physical* **366**, 114993.
2. **Sayem ASM, Lalbakhsh A, Esselle KP, Buckley JL, O'Flynn B and Simorangkir RB** (2022) Flexible transparent antennas: Advancements, challenges, and prospects. *IEEE Open Journal of Antennas and Propagation* **3**, 1109–1133.
3. **Chan J, Iyer V, Wang A, Lyness A, Kooner P, Sunshine J and Gollakota S** (2021) Closed-loop wearable naloxone injector system. *Scientific Reports* **11**, 22663.
4. **Perwej Y, Omer MK, Sheta OE, Harb HAM, and Adrees MS** (2019) The future of Internet of Things (IoT) and its empowering technology. *International Journal of Engineering Science* **9**(3), 20192–20202.
5. **Hong SS, Mehlman J and Katti S** (2012) Picasso: Flexible RF and spectrum slicing. *ACM SIGCOMM Computer Communication Review* **42**, 37–48.
6. **Wheeler HA** (1947) Fundamental limitations of small antennas. *Proceedings of the IRE* **35**, 1479–1484.
7. **Khan MU, Sharawi MS and Mittra R** (2015) Microstrip patch antenna miniaturisation techniques: A review, IET microwaves. *Antennas & Propagation* **9**, 913–922.
8. **Tadesse AD, Acharya OP and Sahu S** (2020) Application of metamaterials for performance enhancement of planar antennas: A review. *International Journal of RF and Microwave Computer-Aided Engineering* **30**, e22154.
9. **Rowell CR and Murch RD** (1997) A capacitively loaded PIFA for compact mobile telephone handsets. *IEEE Transactions on Antennas and Propagation* **45**, 837–842.
10. **Sarrazin F, Pflaum S and Delaveaud C** (2016) Radiation efficiency improvement of a balanced miniature IFA-inspired circular antenna. *IEEE Antennas and Wireless Propagation Letters* **16**, 1309–1312.
11. **Kumar S, Moloudian G, Simorangkir RB, Gawade DR, O'Flynn B and Buckley JL** (2024) Sub-GHz wrist-worn antennas for wireless sensing applications: A review. *IEEE Open Journal of Antennas and Propagation*.
12. **Xu X and Wei J** (2018) Miniaturisation design of patch antenna using a low-profile mushroom type meta-substrate tailored with high permittivity. *IET Microwaves, Antennas & Propagation* **12**, 1216–1221.
13. **Alibakhshikenari M, Ali EM, Soruri M, Dalarsson M, Naser-Moghadasi M, Virdee BS, Stefanovic C, Pietrenko-Dabrowska A, Koziel S and Szczepanski S** (2022) A comprehensive survey on antennas on-chip based on metamaterial, metasurface, and substrate integrated waveguide principles for millimeter-waves and terahertz integrated circuits and systems. *IEEE Access* **10**, 3668–3692.
14. **Yi H, Mu Y, Han J and Li L** (2023) Broadband millimeter-wave metasurface antenna array with printed ridge gap waveguide for high front-to-back ratio. *Journal of Information and Intelligence* **1**, 11–22.
15. **Dey AB, Kumar S, Arif W and Anguera J** (2022) Elastomeric textile substrates to design a compact, low-profile AMC-based antenna for medical and IoT applications. *IEEE Internet of Things Journal* **10**, 4952–4969.
16. **Malekpoor H** (2019) Comparative investigation of reflection and band gap properties of finite periodic wideband artificial magnetic conductor surfaces for microwave circuits applications in X-band. *International Journal of RF and Microwave Computer-Aided Engineering* **29**, e21874.
17. **Malekpoor H and Abolmasoumi A** (2022) High-isolated broadband eight-element linear multi-input multi-output array over artificial magnetic surface for wireless and sub-6 GHz 5G communications. *International Journal of Communication Systems* **35**, e5247.
18. **Foroozesh A and Shafai L** (2010) Investigation into the application of artificial magnetic conductors to bandwidth broadening, gain enhancement and beam shaping of low profile and conventional monopole antennas. *IEEE Transactions on Antennas and Propagation* **59**, 4–20.
19. **Simons RN** (2004) *Coplanar Waveguide Circuits, Components, and Systems*. NASA Glenn Research Center, Cleveland, Ohio: John Wiley & Sons.
20. **Yang X, Huang Y, Dai Z, Barber J, Wang P and Lu N** (2019) "Cut-and-paste" method for the rapid prototyping of soft electronics. *Science China Technological Sciences* **62**, 199–208.

https://doi.org/10.1017/S1759078725000522 Published online by Cambridge University Press

21. **Sievenpiper DF, Zhang L, and Broas R** (1999) High-impedance electromagnetic surfaces with forbidden bands at radio and microwave frequencies. *Terahertz and Gigahertz Photonics*. SPIE's International Symposium on Optical Science, Engineering, and Instrumentation, Denver, CO, United States: SPIE, **3795**, 154–165.
22. **Alqadami ASM, Jamlos MF, Soh PJ and Vandenbosch GA** (2015) Assessment of PDMS technology in a MIMO antenna array. *IEEE Antennas and Wireless Propagation Letters* **15**, 1939–1942.
23. **Technical notes of Double Sided Kapton® Polyimide Tape** https://www.tedpella.com/technote_html/16087-12,%20-19,%20-25%20tn.pdf. Product Numbers 16087-12, 16087-19, and 16087-25 U.S.A / Canada: TED PELLA. INC.
24. **Kassem H, Vigneras V and Lunet G** (2010) Characterization techniques for materials' properties measurement. *Microwave and Millimeter Wave Technologies From Photonic Bandgap Devices to Antenna and Applications*. IntechOpen.
25. **Velan S, Sundarsingh EF, Kanagasabai M, Sarma AK, Raviteja C, Sivasamy R and Pakkathillam JK** (2014) Dual-band EBG integrated monopole antenna deploying fractal geometry for wearable applications. *IEEE Antennas and Wireless Propagation Letters* **14**, 249–252.
26. **Joshi R, Hussin EFNM, Soh PJ, Jamlos MF, Lago H, Al-Hadi AA and Podilchak SK** (2020) Dual-band, dual-sense textile antenna with AMC backing for localization using GPS and WBAN/WLAN. *IEEE Access* **8**, 89468–89478.
27. **Khajeh-Khalili F, Haghshenas F and Shahriari A** (2020) Wearable dual-band antenna with harmonic suppression for application in medical communication systems. *AEU-International Journal of Electronics and Communications* **126**, 153396.
28. **Najumunnisa M, Sastry ASC, Madhav BTP, Das S, Hussain N, Ali SS, and Aslam M** (2022) A metamaterial inspired AMC backed dual band antenna for ISM and RFID applications. *Sensors* **22**, 8065.
29. **Sharma S, Tripathy MR and Sharma AK** (2023) Low SAR dual-band circularly polarized wearable RFID antenna using FSS reflector with reduced EMI. *Progress in Electromagnetics Research C*, 129.
30. **Casula GA, Lestini F, Chietera FP, Muntoni G, Occhiuzzi C, Catarinucci L, Colella R, Montisci G, and Marrocco G** (2024) Design of on-body epidermal antenna on AMC substrate for UHF RFID in healthcare. *IEEE Transactions on Antennas and Propagation* **72**, 4023–4035.

Elie Zaraket is a Ph.D. student. In 2020, he received a Master's degree in Microsystems and Embedded Systems in the Faculty of Sciences in Lebanese University, Lebanon. In 2021, he works on the modeling, Design and Characterization of Energy-Data Hybrid Transition Device at EnergyLab of the University of La Réunion in collaboration with NUIST, Nanjing, China. Currently, he is pursuing his thesis in radiofrequency field at IMS Laboratory of the University of Bordeaux, France.

Ludivine Fadel received the Ph.D. degree in Electrical Engineering from the University of Bordeaux, France, in 2004. She is an Associate Professor at Bordeaux University and her main research interests include wireless power transfer and energy harvesting, materials and printing technologies for RF application.

Yéro Dia is currently pursuing his thesis in electromagnetic energy harvesting on flexible substrates for powering WBAN networks. In 2021, he received a Master's degree in Microsystems, Instrumentation and Robotics in University of Franche-Comté, in Besançon, France.

Valérie Vignéras is a full professor in the Polytechnic Institute of Bordeaux and conducts research in the IMS Laboratory on complex structures (mixtures, structured media, and self assembled media) both by simulation to predict or optimize their properties and by characterization before their integration in high-frequency systems (antennas, electromagnetic compatibility, and radar shieldness).

Laurent Oyhénart received the Ph.D. degree in Electrical Engineering from the University of Bordeaux, Bordeaux, France, in 2005. Currently he is an Associate Professor with the University of Bordeaux and develops his research activities in the IMS Laboratory. His research interests include computational electromagnetics, photonic crystals, and antenna synthesis.

https://doi.org/10.1017/S1759078725000522 Published online by Cambridge University Press